

## SUPPLEMENTAL MATERIAL

This Supplemental Material accompanies the manuscript “Past Eruptions of a Newly Discovered Active Shallow Silicic Submarine Volcano Near Tokyo Bay, Japan” by McIntosh et al.

It contains further details regarding the following topics:

- i Submarine sampling details
- ii Tephra sampling locations, characteristics and geochemistry
- iii Volatile analysis by FTIR
- iv Density and porosity analysis
- v Sample volatile and porosity data
- vi Calculation of expected OH content vs pressure and water depth
- vii Producing a region-specific sea level curve
- viii Details of uncertainties in lava age estimates

Additional spreadsheets with full FTIR data (absorbance, glass thickness, etc) and pumice geochemistry data are also included in the Data Repository.

### i Submarine sampling details

Sampling details including water depth are given in Table S1. Additional cruise information can be found online in JAMSTEC’s Data and Sample Research System for Whole Cruise Information (DARWIN) database at <http://www.godac.jamstec.go.jp/darwin/e> or by contacting the corresponding author, Iona McIntosh, at [i.m.mcintosh@jamstec.go.jp](mailto:i.m.mcintosh@jamstec.go.jp)

*Table S1. Submarine sampling details*

Cruise	ROV dive	Sample	Description	Latitude (N)	Longitude (E)	Sampling depth (mbsl)
KS-16-6	HPD1970	#1970-R01	In-place lava	34 ° 31.913'	139 ° 26.047'	94
NT07-15	HD719	#719-R14	In-place lava	34 ° 32.6'	139 ° 26.622'	106
NT12-19	HPD1409	#1409-R10	Loose pumice	34 ° 32.337'	139 ° 26.876'	118
NT12-19	HPD1407	#1407-R01	Loose pumice	34 ° 33.555'	139 ° 30.138'	194

## ii Tephra sampling locations, characteristics and geochemistry

Subaerial tephra layer O58 was sampled at 34.701480°N, 139.377038°E in Senbazaki, SW Izu-Oshima at the ‘Great Road Outcrop’ described in Uesugi et al. (1994). The subaerial tephra layer O3T on Toshima island was sampled at 34.531625°N, 139.276201°E in Toshima Port, below the ~8 ka Kajiana lava flow described by Isshiki (1978) and between the two <sup>14</sup>C-dated layers reported in Oikawa and Tani (2020).

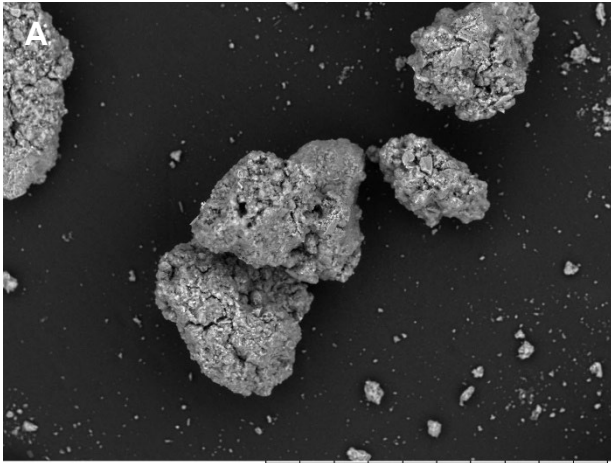
Tephra samples were dried at room temperature over several days by monitoring their changing weight until mass loss due to drying had ceased. Samples were then dry sieved. Tephra sampled from O3T and the center of the O58 deposit contained pumice clasts and fine-grained matrix only; tephra sampled from the base of O58 also contained dense angular lithics ≤1 cm in size (comprising 5% by mass) (Fig. S1).



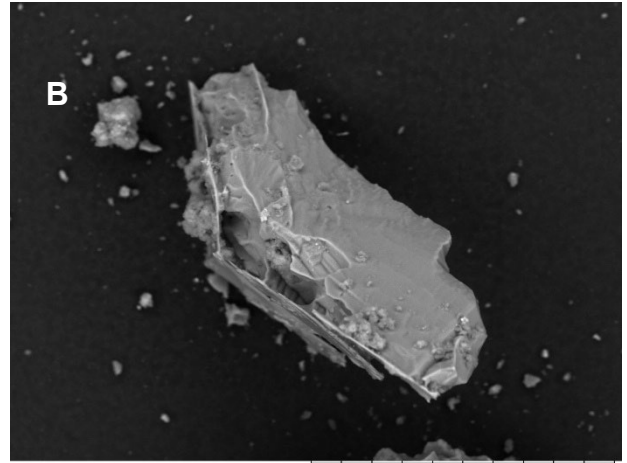
*Figure S1. Example of dense angular lithics from lower part of O58 tephra layer.*

Particle aggregates in the fine-grained matrix could not be broken up even when very firm pressure was applied. For comparison, ‘damp’ tephra straight from the outcrop were also sieved in the same way, and exhibited the same particle aggregates. These particle aggregates could not be disaggregated even when immersed in water and placed in an ultrasonic bath. SEM images reveal that aggregates include extremely fine (<20 μm) material. The fine-grained matrix also contains blocky avescicular and weakly vesicular shards, some of which exhibit stepped features or manganese films (Fig. S2).

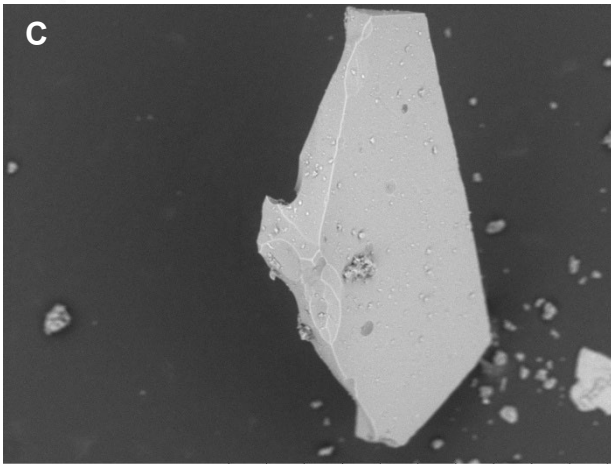
Tephra pumice clasts were mounted in epoxy, polished, and analyzed for major and trace elements by laser ablation (LA-) inductively coupled plasma mass spectrometer (-ICP-MS) at the Japan Agency for Marine-Earth Science and Technology (JAMSTEC) using a modified Element XR sector field ICP-MS following the method of Kimura and Chang (2012). Oomuro Hole rhyolite lava (sample #719-R05), a weakly pumiceous glassy lava with low crystal content, was prepared as sample slabs (<200 g) that were then coarsely crushed in a tungsten carbide mortar and further pulverized in an alumina mill. Brine contamination was removed by repeatedly boiling samples in distilled water prior to crushing. Major element compositions were measured using X-ray fluorescence (XRF) spectrometer (RIGAKU SIMULTIX12) on fused glass beads (Tani et al., 2005). The sample powders were ignited at 900 °C for 4 hours, and then 0.4 g of sample powders were mixed with 4.0 g of lithium tetraborate flux to make glass beads. Concentrations of trace elements were determined by ICPMS using an Agilent 7500s system (Chang et al., 2003). The sample



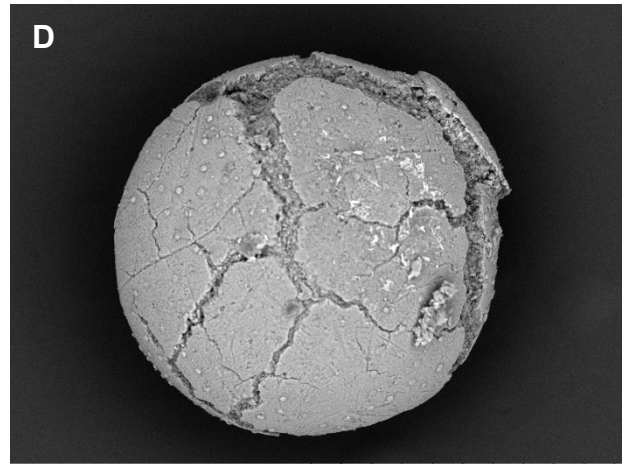
Miniscope6091 2018/02/28 12:06 HL D4.1 x300 300 um  
730Top x40



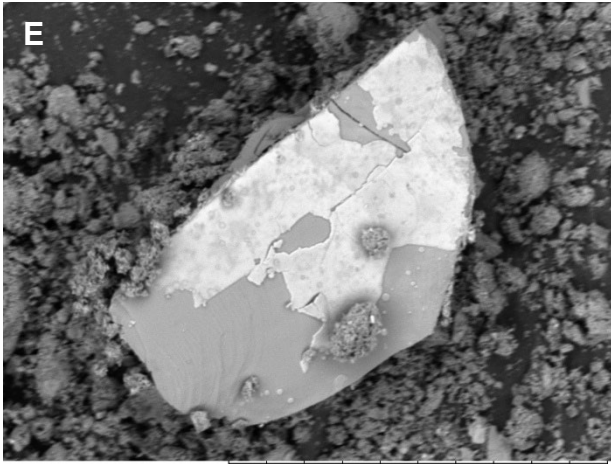
Miniscope6092 2018/02/28 12:19 HL D4.2 x800 100 um  
730Top x40



Miniscope6100 2018/02/28 15:11 FL D3.7 x1.0k 100 um  
730Top x40



Miniscope2817 2014/12/06 20:24 NL D5.5 x400 200 um  
730Top x40



Miniscope6136 2018/04/18 13:52 F D5.2 x1.0k 100 um  
730Top x40

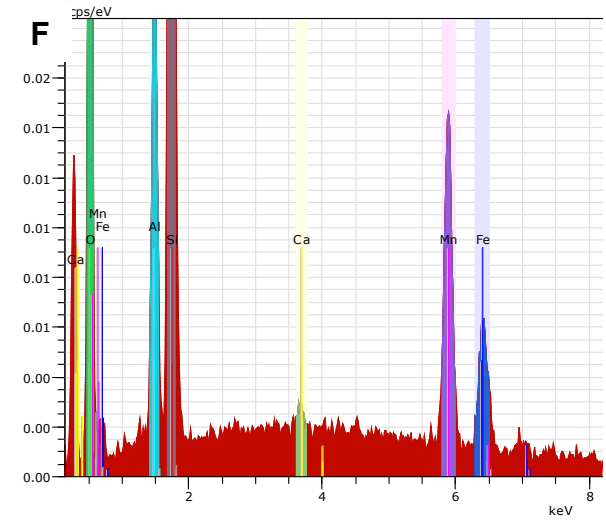


Figure S2. Additional SEM images of tephra. A) particle aggregates B) particle with stepped features C) dense blocky particle D) possible accretionary lapilli E) particle with manganese coating on one face (i.e. likely formed prior to fragmentation and deposition) F) EDS spectrum of manganese coating in E.

powders (~0.1 g) were dissolved in acid digestion bombs for 120 hours under 180°C following the methods described by Takei et al. (2001) and Tanaka et al. (2003).

Geochemical data for the pumice clasts from the O58 and O3T tephra layers are shown in Figure S3 compared to the published geochemical data for the nearby rhyolitic volcanic islands Niijima and Kozushima that could be other potential sources for the tephra layers. Trace element data are normalized to primitive mantle values of Sun and McDonough (1989). Data for Kozushima and Niijima are taken from Taylor and Nesbitt (1998), Isshiki (1982) and Isshiki (1987). Major and trace element geochemistry for pumice from both tephras overlie the rhyolite from Oomuro Hole and are distinct from neighboring rhyolitic centers.

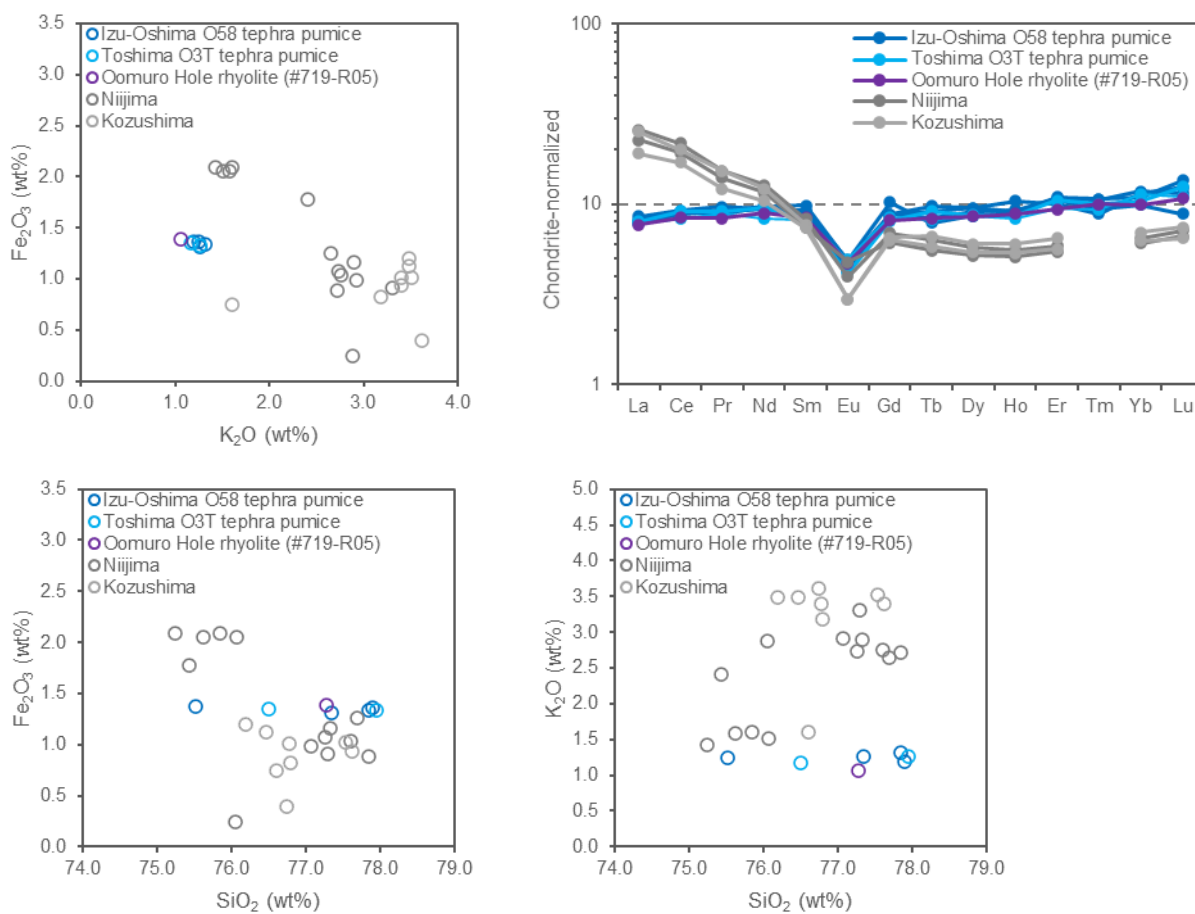


Figure S3. O58 and O3T tephra geochemistry compared with geochemistry of Oomurodashu rhyolite and other potential regional rhyolitic sources (Niijima and Kozushima).

### iii Volatile analysis by FTIR

FTIR sample preparation and analysis was undertaken at JAMSTEC following the methods of McIntosh et al. (2017) and Mitchell et al. (2018), which make it possible to analyze vesicular and/or hydrated glasses.

Where possible matrix glasses were prepared as double polished wafers of uniform thickness. To produce wafers, samples were attached to glass slides using Crystalbond 509 and then ground on successively fine silica carbide paper to produce a flat surface. A final polish was achieved by polishing briefly with 3  $\mu\text{m}$  and 1  $\mu\text{m}$  diamond paste on a polishing pad. Glass slides were then placed briefly (<5 s) on a  $\sim 160$  °C hot plate to soften the Crystalbond sufficiently to turn the sample over. The second side was then ground and polished as before. Wafers were detached from glass slides by dissolving the Crystalbond with acetone. After cleaning in a second acetone bath, delicate wafers were removed from acetone using tweezers or a fine brush and stored in gelatin capsules until analysis. Usually however vesicular glasses could not be prepared as wafers (due to their fragility and the difficulty of fully removing Crystalbond from vesicle edges, which produces a contamination peak at  $\sim 1730$   $\text{cm}^{-1}$ ). Instead vesicular glasses were lightly crushed to produce glass shards. Suitable shards (near-flat without internal bubbles) were then selected for analysis.

Analyses were conducted using JAMSTEC's Varian FTS Stingray 7000 Micro Imager Analyzer spectrometer with an attached UMA 600 microscope. Mid-IR (6000-700  $\text{cm}^{-1}$ ) images were collected at a spectral resolution of 8  $\text{cm}^{-1}$  using a ceramic (globar) infrared source, a Ge-coated KBr beamsplitter, and the liquid nitrogen-cooled Varian Inc. Lancer Focal Plane Array (FPA) camera housed in the microscope. The FPA camera consists of 4096 infrared photovoltaic HgCdTe<sub>2</sub> (MCT) detector pixels (arranged 64  $\times$  64) that image a 350  $\times$  350  $\mu\text{m}$  area of the sample, producing a pixel resolution of  $\sim 5.5 \times 5.5$   $\mu\text{m}$ . The FPA camera was calibrated regularly. Samples were placed on an IR-transparent KBr window under N<sub>2</sub> purge for analysis. An initial background image of the KBr window was collected then subtracted automatically from each sample image; new background images were taken approximately every 300 min. Each image (comprising 512 scans) takes  $\sim 15$  min to acquire. Each sample area was imaged in transmission then reflectance mode (i.e. without moving the stage) before moving to the next area for analysis.

Images were processed using Varian Win-IR Pro software (v3.3.1.014). For wafers of uniform thickness, images of species absorbance show changes in relative concentration. Note that thin (<30  $\mu\text{m}$ ) wafers may exhibit interference fringes in their transmission spectra, leading to the appearance of minor, rhythmic variations in images of species absorbance produced using a fixed peak baseline (e.g. Fig. 3B). For glass shards, individual pixels with good spectra in both transmission and reflectance were selected and processed as individual spot analyses with  $\sim 5.5 \times 5.5$   $\mu\text{m}$  resolution. Glass thickness was then calculated from frequency of interference fringes in the reflectance spectra (e.g. Nichols and Wysoczanski, 2007), using a refractive index of 1.5 for rhyolite (Long and Friedman, 1968). Species absorbance was found from corresponding transmission spectra as peak height above a baseline. For glass shards, non-linear baselines required transmission spectra to be exported and printed, with baselines drawn by hand using a flexicurve. For reference, flexicurve baselines drawn for the H<sub>2</sub>O<sub>t</sub> and H<sub>2</sub>O<sub>m</sub> peaks in an example spectrum from crater lava #719-R14 are shown in Figures S5 and S6. H<sub>2</sub>O<sub>m</sub> concentrations were calculated in the standard manner by entering the absorbance of the 1630  $\text{cm}^{-1}$  H<sub>2</sub>O<sub>m</sub> peak into the Beer-Lambert law (Stolper, 1982b), using a molar absorptivity coefficient for rhyolite of  $55 \pm 2$  l mol<sup>-1</sup> cm<sup>-1</sup> (Newman et al., 1986) and glass density of 2350 g/cm<sup>3</sup>. H<sub>2</sub>O<sub>t</sub> and OH concentrations were calculated from the 3500  $\text{cm}^{-1}$  H<sub>2</sub>O<sub>t</sub>

peak using the modified Beer-Lambert law method of McIntosh et al. (2017), which accounts for the species-dependence of the  $3500\text{ cm}^{-1}$   $\text{H}_2\text{O}_t$  molar absorptivity coefficient  $\epsilon_{3500}$ .  $\text{CO}_2$  was below detection limits for all samples. Detection limits are inversely proportional to sample thickness; for the thickest glasses ( $\sim 40\text{ }\mu\text{m}$ )  $\text{CO}_2$  detection limits are 16 ppm, using a molar absorptivity coefficient of  $1214\text{ l mol}^{-1}\text{ cm}^{-1}$  for the  $2350\text{ cm}^{-1}$   $\text{CO}_2$  peak (Behrens et al., 2004).

The largest error on FTIR concentrations for thin glasses is usually derived from the error on determining glass thickness from reflectance spectra, typically reported as  $\pm 3\text{ }\mu\text{m}$  (Nichols and Wysoczanski, 2007), which can give errors of  $\pm 15\%$  relative for thin ( $< 20\text{ }\mu\text{m}$ ) samples. Here there is additional uncertainty on measured absorbances from non-linear baselines in transmission spectra, either due to curvature caused by non-parallel shards, or (ironically) by the appearance of interference fringes for thin, parallel wafers. Comparison of absorbances measured using flexicurve and linear baselines for the same spectra show that this potential error falls within the  $\pm 15\%$  relative error quoted for thickness. Errors on OH data are therefore reported as  $\pm$  standard deviation of the mean for all analyzed spectra for a particular sample. Reported OH data are bulk data for each sample (for individual spot analyses see accompanying spreadsheet of FTIR data); it is therefore possible that they reflect some natural heterogeneity in OH within the sample. OH heterogeneity could relate to concentration profiles around bubbles formed by diffusive bubble growth during degassing prior to eruption, or by hydration during slow cooling that enabled some interconversion of added  $\text{H}_2\text{O}_m$  to OH prior to reaching  $T_g$ .

#### iv Density and porosity analysis

Bulk density and porosity were obtained via the Archimedes method after wrapping clasts tightly in parafilm. Additional He-pycnometry measurements were made to assess the proportions of isolated versus connected porosity; all clasts had  $< 5\%$  isolated porosity.

#### v Sample volatile and porosity data

Data are given in Table S2.

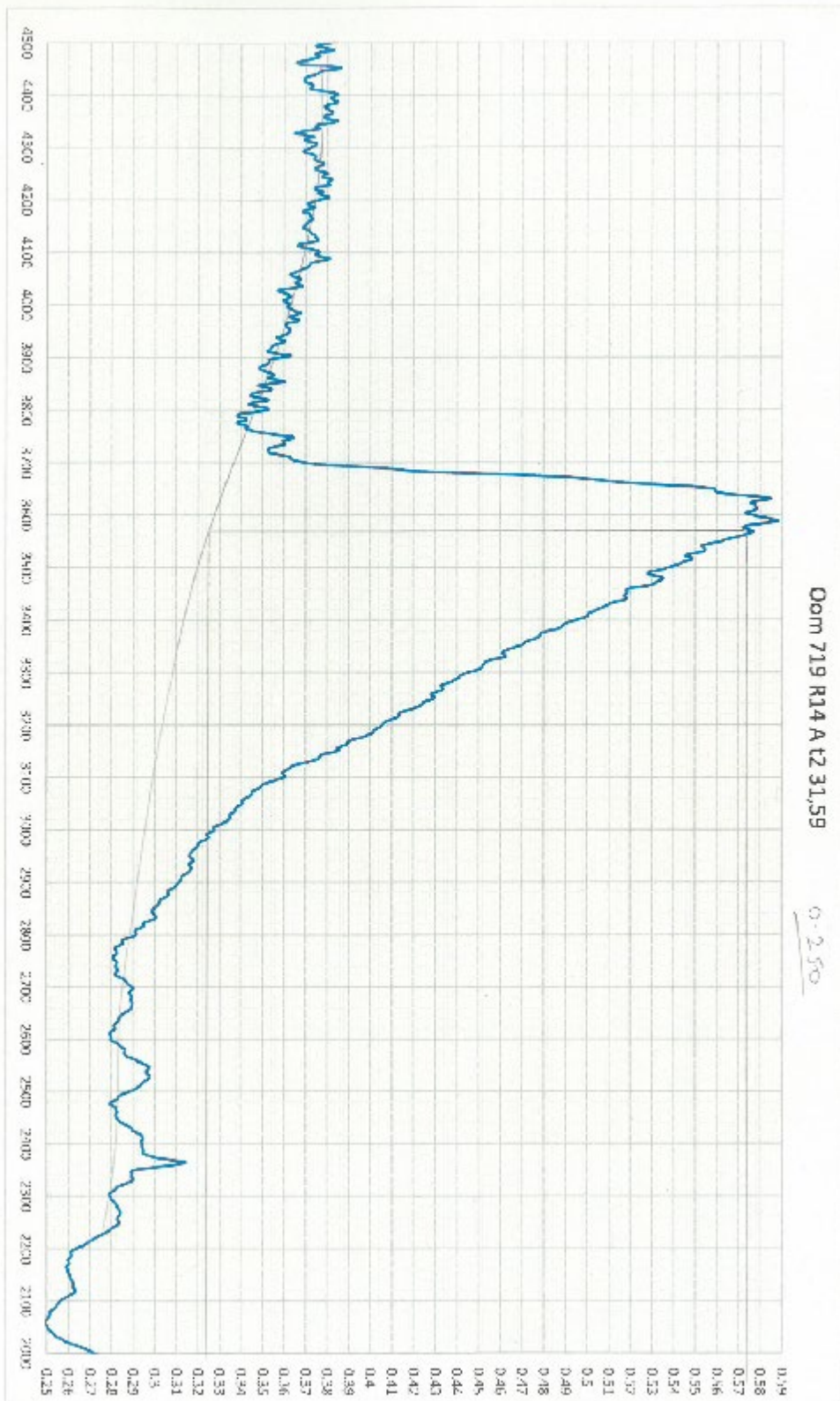


Figure S5. Flexicurve baseline drawn by hand for the  $3500\text{ cm}^{-1}$   $\text{H}_2\text{O}_l$  peak in an example FTIR spectrum from crater lava #719-R14.

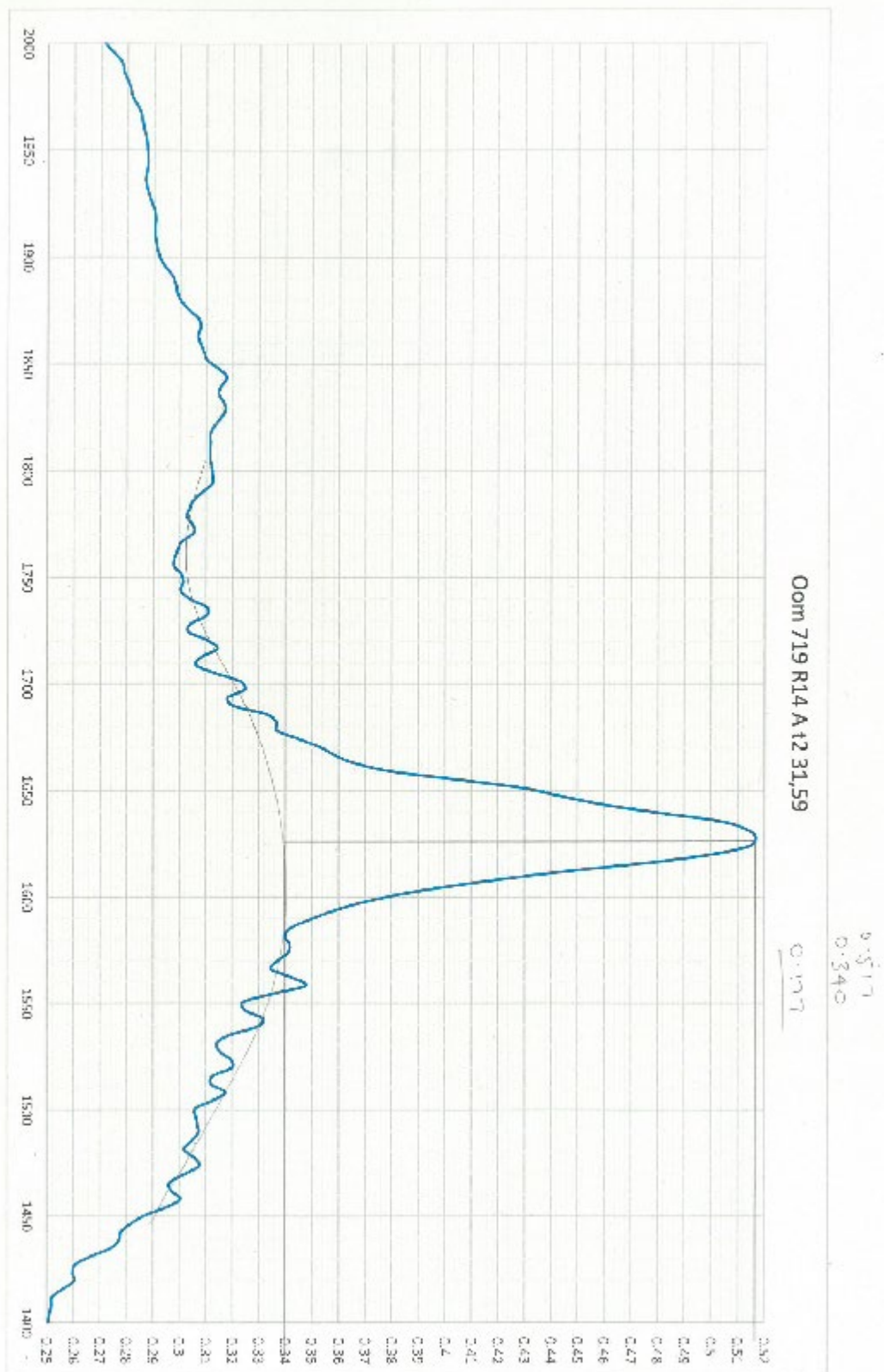


Figure S6. Flexicurve baseline drawn by hand for the 1630 cm<sup>-1</sup> H<sub>2</sub>O<sub>m</sub> peak in an example FTIR spectrum from crater lava #719-R14.

Table S2. Sample porosity and volatile data

Sample	Bulk density (kg/m <sup>3</sup> )	Total porosity (%)	FTIR data (wt%) standard deviation						Note
			H <sub>2</sub> O <sub>t</sub>	$\sigma$	H <sub>2</sub> O <sub>m</sub>	$\sigma$	OH	$\sigma$	
#1970-R01	1533.7	37	0.41	0.11	0.09	0.12	0.32	0.02	
#719-R14	1724.6	29	1.53	0.24	1.22	0.20	0.31	0.09	
#1409-R10	1614	33	0.77	0.38	0.46	0.39	0.31	0.03	
#1407-R01	666.3	72	0.24	0.01	0.02	0.00	0.22	0.01	average of far-field spots away from hydrated bubble margins
O58_a	1000	59	2.13	0.74	1.5	0.51	0.63	0.24	
O58_b	-	-	1.84	0.69	1.22	0.57	0.62	0.25	porosity not measured prior to FTIR analysis
O3T	642.9	73	1.81	0.71	1.32	0.53	0.49	0.23	

## vi Calculation of expected OH content vs pressure and water depth

Expected OH vs pressure curves are based on the variation in  $H_2O_t$  with pressure for rhyolite at 800 °C (Newman and Lowenstern, 2002). For each output  $H_2O_t$ , pressure data point, equivalent OH contents at  $T_g$  are calculated via an  $H_2O$  speciation model for rhyolite (Nowak and Behrens, 2001) assuming  $T_g$  values of 800 °C (i.e. instant quench) to 600 °C. Pressures are converted to depth below sea level assuming a hydrostatic pressure gradient with seawater density of 1025 kg/m<sup>3</sup>. For calculating depth in the volcanic conduit, a density of 2300 kg/m<sup>3</sup> is used.

## vii Producing a region-specific sea level curve

Models of past sea level rise must account for the global change in ice equivalent volume and also for local tectonic processes affecting relative sea level. The Izu-Bonin arc is actively colliding with mainland Japan, leading to uplift in the Tokai region. We therefore adapt the global sea level curve of Lambeck et al. (2014) for the average uplift of 0.86 mm/yr calculated for the Tokai region (Okuno et al., 2014), producing a sea level curve (Fig. S7) that reproduces the magnitude and timing of the late Holocene high stand observed in the region (Fujii and Fuji, 1967; Umitsu, 1991). This adjusted model also gives a low stand of ~120 m below current sea level at the Last Glacial Maximum (~20 ka), which corresponds to the current depth of the flat Oomurodashi summit that is thought to have been produced by wave planation during this time.

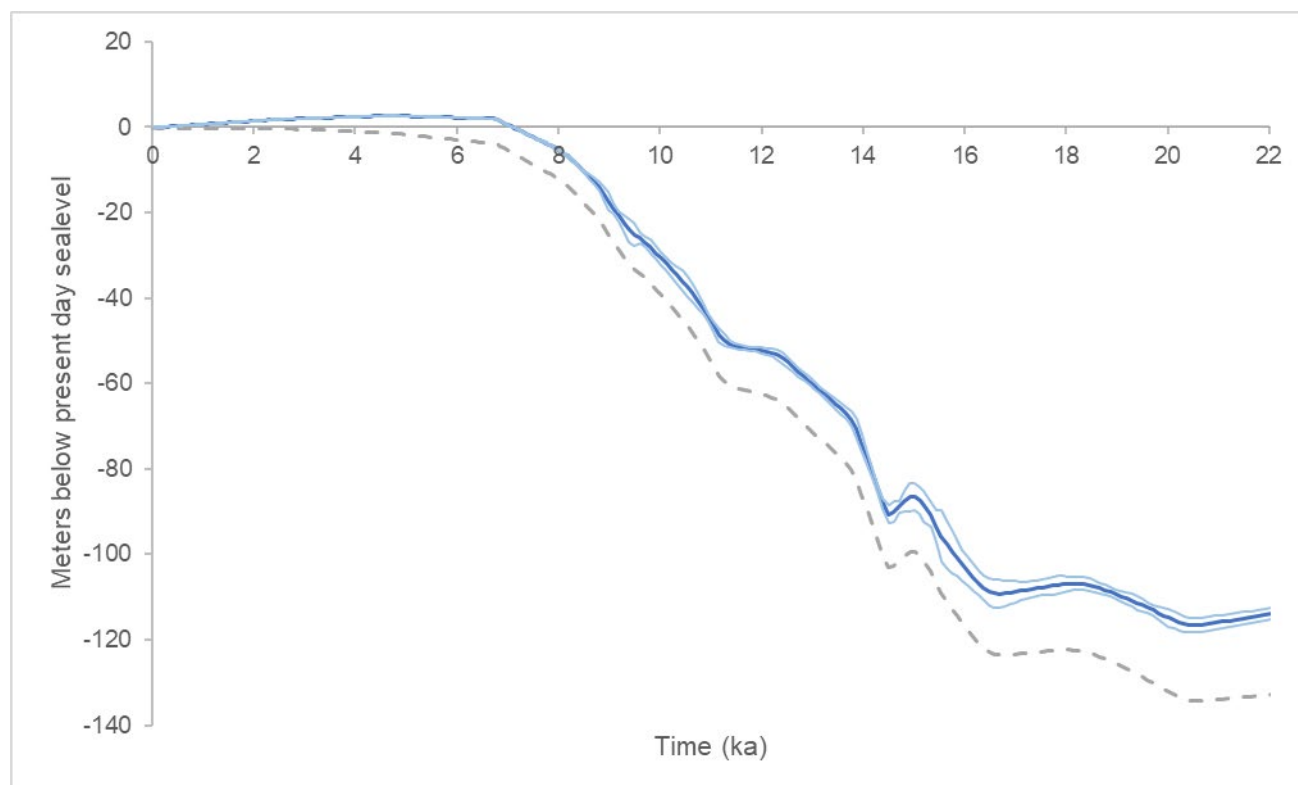


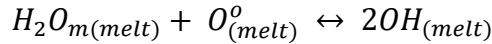
Figure S7. Sea level curve of Lambeck et al. (2014) adjusted assuming average uplift of 0.86 mm/yr shown in blue; light blue indicates error on original curve. Grey dashed curve shows original Lambeck et al. (2014) model for comparison.

## viii Discussion of uncertainties on lava age estimates

The link between lava volatile contents and past sea level rise has the potential to be used to date late Quaternary submarine lava flows around the world. Here we discuss uncertainties of the method and the relative magnitude of their impacts, with reference to the data for Oomurodashi's crater lava (#719-R14) and summit lava knoll (#1970-R01).

### *Glass transition temperature ( $T_g$ ) assumption for hydrated glasses*

Water exists in melts and glasses as two species – molecular water ( $H_2O_m$ ) and hydroxyl groups (OH) – that interconvert according to the reaction:



in which  $H_2O_m$  reacts with bridging oxygen atoms ( $O^o$ ) to produce OH groups that are bound to the silicate framework (Stolper, 1982a). For a given  $H_2O_t$  content the position of this reaction varies with temperature, with the equilibrium position shifted toward the right (more OH) at higher temperatures and toward the left (less OH) at lower temperatures. When a lava with a given  $H_2O_t$  content is erupted on the seafloor and begins to cool, its OH content will begin to decrease as the equilibrium position of the interconversion reaction shifts to the left. However, the interconversion reaction rate decreases dramatically with temperature (Zhang et al., 1991, 1995) so it takes an increasingly long time for  $H_2O_m$  to interconvert to OH as the lava cools. At a certain temperature, the reaction rate becomes negligible and there is no further interconversion with further cooling, i.e. the species concentrations become fixed. This is the temperature of apparent equilibrium,  $T_{ae}$ , which is equivalent to the lava's glass transition temperature ( $T_g$ ) (Dingwell and Webb, 1990; Zhang et al., 1997). Although low temperature secondary hydration in the time after eruption may add  $H_2O_m$  thus increasing the  $H_2O_t$  content of a glass, there is no interconversion of this additional  $H_2O_m$  to OH because the interconversion reaction rate remains negligible. The OH content of a lava therefore becomes fixed at  $T_g$ .

Each lava will have a different  $T_g$  value according to its  $H_2O_t$  content and its cooling rate, with higher  $T_g$  for lower  $H_2O_t$  content and/or fast cooling, and lower  $T_g$  for higher  $H_2O_t$  content and/or slow cooling. Interpreting OH contents in terms of a degassing model (where  $H_2O_t$  and thus OH decreases as pressure decreases) requires knowledge of the individual lava's  $T_g$  value. In unhydrated glasses, the concentrations of  $H_2O_m$  and OH themselves record  $T_g$  (as  $T_{ae}$ ), because it is known from experimental studies how  $H_2O$  species concentrations vary with  $H_2O_t$  for different temperatures (e.g. Nowak and Behrens, 2001). In hydrated glasses with excess  $H_2O_m$ , however,  $T_g$  must be assumed.

For a measured OH content, a lower assumed  $T_g$  will relate it to a higher (pre-hydration)  $H_2O_t$  content at eruption and therefore to a higher emplacement pressure. The minimum emplacement pressure is found by assuming instant quench to glass i.e.  $T_g =$  eruption temperature. For estimating lava ages, this means that a lower assumed  $T_g$  gives deeper water depths when lavas were emplaced, hence younger ages due to the general trend of increasing sea level since the Last Glacial Maximum. Maximum lava ages will therefore be found by assuming instant quench and high  $T_g$ . The  $T_g$ -related age uncertainty varies according to where the volatile-based age lies on the curve of past sea-level: for periods of rapid sea level rise (e.g. 8 - 16 ka) the age uncertainty is small; for periods of small or gradual sea level change (e.g. 0 - 7 ka) then the age uncertainty is potentially much larger.

For comparison, Table S3 shows the variation in eruption age for Oomurodashi's summit knoll and crater lavas for assumed  $T_g$  values of 800 °C (i.e. instant quench), 700 °C and 600 °C. For each lava,

the variation in eruption age for  $T_g = 800\text{-}600\text{ }^\circ\text{C}$  is  $<1$  ka. Cooling rates of submarine rhyolite lavas are not constrained, but they are expected to be faster than equivalent flows cooling in air, which would favour higher  $T_g$ . Oomurodashi's shallow summit (hence low emplacement pressure) means these lavas had degassed to low  $\text{H}_2\text{O}_t$  contents, which would also favour higher  $T_g$ . We therefore assumed a  $T_g$  of  $700\text{-}800\text{ }^\circ\text{C}$  when estimating these lava ages.

Table S3. Effect of  $T_g$  assumption on estimated lava ages.

	Mean OH wt% ( $\pm\sigma$ )	Sampling depth (mbsl)	Eruption depth (mbsl) & Relative Sea Level (m) assuming:						Eruption age (ka) assuming:		
			$T_g$ 800	RSL	$T_g$ 700	RSL	$T_g$ 600	RSL	$T_g$ 800	$T_g$ 700	$T_g$ 600
Summit knoll #1970-R01	$0.32 \pm 0.02$	94	77	-17	80	-14	87	-7	9.0	8.8	8.2
Crater lava #719-R14	$0.31 \pm 0.09$	106	71	-35	75	-31	81	-25	10.4	10.0	9.5

youngest combination	oldest combination
----------------------	--------------------

#### Analytical uncertainty on OH measurement

The use of the species-dependent  $\epsilon 3500$  FTIR method for mid-IR analysis (McIntosh et al 2017) overcomes the issues related to the previous method of finding OH-by-difference (i.e.  $\text{OH wt}\% = \text{H}_2\text{O}_t \text{ wt}\% - \text{H}_2\text{O}_m \text{ wt}\%$ ) when using a fixed  $\epsilon 3500$  value for the  $\text{H}_2\text{O}_t$  peak. Thus, one of the major obstacles to use of OH contents measured with mid-IR FTIR analysis has now been removed. For thin ( $<20\text{ }\mu\text{m}$ ) samples the  $\pm 3\text{ }\mu\text{m}$  error on the thickness measurement (obtained from interference fringes in reflectance spectra) is typically much larger than the uncertainties related to  $\epsilon$  values, glass density and absorbance (peak height above baseline). In such cases it is common to use this thickness uncertainty to calculate overall FTIR analytical uncertainty (as in Fig. 3C). However, given the importance of the OH measurement for interpreting lava ages, we take a more conservative approach by using  $\pm 1\text{ }\sigma$  of the mean OH value as the analytical uncertainty on OH wt%. This  $\pm 1\text{ }\sigma$  uncertainty is equal to or greater than the uncertainty relating to thickness. It is also greater than the uncertainty on the absorbance measurement for spectra requiring hand-drawn flexicurve baselines.

Table S4. Effect of analytical uncertainty on estimated lava ages.

	Adjusted OH wt%	Sampling depth (mbsl)	Eruption depth (mbsl) & Relative Sea Level (m) assuming:				Eruption age (ka) assuming:	
			$T_g$ 800	RSL	$T_g$ 700	RSL	$T_g$ 800	$T_g$ 700
Summit knoll #1970-R01	Mean OH + $\sigma$	0.34	89	-5	93	-1	8.0	7.3
	Mean OH - $\sigma$	0.30	66	-28	69	-25	9.8	9.5
Crater lava #719-R14	Mean OH + $\sigma$	0.40	128	22	135	29	*	*
	Mean OH - $\sigma$	0.22	30	-76	32	-74	14.0	14.0

youngest combination	oldest combination	* regional RSL never exceeds +3m
----------------------	--------------------	----------------------------------

Higher OH values relate to higher pressure/deeper water depths at eruption and thus to younger lava ages. Mean OH wt% +  $1\text{ }\sigma$  will therefore give younger ages while mean OH wt% -  $1\text{ }\sigma$  will give older lava ages. Table S4 shows that for Oomurodashi, combining the  $\pm 1\text{ }\sigma$  analytical uncertainty with the assumed  $T_g$  range of  $800\text{ - }700\text{ }^\circ\text{C}$  gives an age of  $7.3\text{ - }9.8$  ka for summit knoll lava #1970-

R01, and an age of 0 – 14.0 ka for crater lava #719-R14. For the crater lava, its large  $\sigma$  gives an upper OH bound that leads to calculated relative sea level values that exceed the late Holocene high stand in the region. From volatile data we therefore present a maximum age for this lava, and use the cross-cutting relationships of the formation of the Oomuro Hole crater to constrain its minimum age to 13.2-13.8 ka.

### *Incomplete (disequilibrium) degassing*

The assumption that lava  $H_2O_t$  (hence OH) contents record their emplacement pressure requires that the magma underwent equilibrium degassing i.e. was able to efficiently exsolve  $H_2O$  as  $H_2O$  solubility in the melt decreased with decreasing pressure. However, some magmas may undergo disequilibrium degassing if the rate of volatile exsolution cannot keep pace with the pressure decrease. If such a magma was erupted and quickly quenched before melt  $H_2O_t$  contents could equilibrate with the ambient pressure, the lava would retain some amount of excess  $H_2O_t$  hence excess OH. Incompletely equilibrated lavas containing excess OH will therefore be older than their estimated ages, because higher OH indicates higher pressure/deeper water thus younger age.

Table S5 compares the calculated eruption ages for the two Oomurodashi lavas assuming hypothetical disequilibrium degassing with excess OH of 0.1 and 0.15 wt%. For the summit knoll the maximum age (for  $T_g = 800$  °C) would increase from 9.8 to 13.4 or 14.2 ka for 0.1 or 0.15 wt% excess OH, respectively; for the crater lava the maximum age would increase from 14.0 to 14.1 or 15.5 ka, respectively. The impact of this hypothetical excess OH is smaller for the crater lava because it lies on a steeper section of the past sea level curve.

*Table S5. Effect of potential incomplete degassing on estimated lava ages.*

		Adjusted OH wt%	Sampling depth (mbsl)	Eruption depth (mbsl) & Relative Sea Level (m) assuming:				Eruption age (ka) assuming:	
				Tg 800	RSL	Tg 700	RSL	Tg 800	Tg 700
Summit knoll #1970-R01	<b>0.1 wt% excess OH</b>	0.22	94	30	-64	32	-62	13.4	13.2
	<b>0.15 wt% excess OH</b>	0.17		14	-80	14	-80	14.2	14.2
Crater lava #719-R14	<b>0.1 wt% excess OH</b>	0.21	106	27	-79	28	-78	14.1	14.1
	<b>0.15 wt% excess OH</b>	0.16		11	-95	11	-95	15.5	15.5

<i>youngest combination</i>	<i>oldest combination</i>
-----------------------------	---------------------------

Are the Oomurodashi lavas likely to retain this much excess OH? Comparison with subaerial lavas is instructive. Comprehensive  $H_2O_t$  data (from manometry analyses) are available for the dacite lavas from the lava domes at Santiaguito and Mt St Helens (Anderson and Fink, 1989; Anderson et al., 1995). These studies compared samples with smooth (<30% bubbles) and scoriaceous (>50% bubbles) textures, from flow interiors and exteriors, and from proximal and distal to the vent. Anderson and Fink (1989) showed that for a given distance from the vent, scoriaceous samples had lower  $H_2O_t$  than smooth samples; and for a given texture, flow-front samples had lower water contents than near-vent samples. Overall, flow front samples (both textures) had  $0.13 \pm 0.05$  ( $\sigma$ ) wt%  $H_2O_t$  while near vent samples (both textures) had  $0.18 \pm 0.03$  ( $\sigma$ ) wt%  $H_2O_t$ . Anderson et al 1995's detailed study of the October 1986 lobe at Mt St Helens (all smooth low vesicularity lava) also found the highest  $H_2O_t$  at the vent, with 0.22 wt%  $H_2O_t$  at 2.5 m from the vent; however for all samples >10 m from the vent the mean  $H_2O_t$  was  $0.14 \pm 0.02$  ( $\sigma$ ) wt%. Their data for exogenous flows at

Santiaguito (all smooth, low vesicularity samples) give mean  $H_2O_t$  for all distal samples of  $0.10 \pm 0.04$  ( $\sigma$ ) wt%, compared with  $0.12 \pm 0.03$  ( $\sigma$ ) wt% for all near-vent samples. The highest value recorded at Santiaguito was 0.19 wt%  $H_2O_t$  for a near-vent sample. Together, all these data suggest that the volatile contents of subaerial flows can equilibrate to atmospheric pressure, with the best candidates for equilibrated samples being higher vesicularity flow exteriors from distal parts of the flow. Meanwhile, incompletely equilibrated samples may be found within  $\sim 10$  m of the vent, where glass may retain an excess of up to 0.1 wt%  $H_2O_t$ .

Although submarine lavas may cool faster than subaerial lavas that cool in air, they are erupted at higher pressure and therefore have higher  $H_2O_t$  contents than subaerial lavas. Higher  $H_2O_t$  content favours lower  $T_g$  values and faster  $H_2O$  diffusion (as  $H_2O_t$  diffusivity is concentration-dependent). These factors will increase the ability of submarine lavas to exsolve  $H_2O$  efficiently and equilibrate with ambient pressure at eruption. The sample for the summit knoll lava #1970-R01 was a flow exterior with 37% vesicularity. We therefore consider it likely to have fully equilibrated with its emplacement pressure. When calculating its age we therefore propagate its  $\pm\sigma$  error on OH but do not assume any excess OH from incomplete degassing. By contrast, the sample for crater lava #719-R14 was taken from the cross-sectioned flow interior and had a vesicularity of 29%. It is therefore possible that this sample may not be fully equilibrated with its emplacement pressure. Taking the maximum  $\sim 0.1$  wt% excess  $H_2O_t$  seen in the subaerial samples as a guide and assuming the same for the crater lava only increases its maximum age (i.e. assuming instant quench with  $T_g = 800$  °C) from 14.0 to 14.1 ka; assuming as much as 0.15 wt% excess OH would increase its maximum age to 15.5 ka.

#### Past sea level curve

Late Quaternary tectonic uplift in the Tokai region has been well constrained at 0.86 mm/yr and our uplift-adjusted model for past sea level rise is in good agreement with the depth of Oomurodashi's wave-planated flat summit; we are therefore confident in using this model to estimate the lava ages. For reference, Table S6 compares the apparent lava ages for the Oomurodashi lavas assuming hypothetical tectonic uplift rates of 0, 1, and 2 mm/yr. This range of uplift rates would change calculated ages by  $<2$  ka.

Table S6. Effect of uplift-adjusted past sea level curve on estimated lava ages.

		Mean OH (wt%)	Sampling depth (mbsl)	Eruption depth (mbsl) & Relative Sea Level (m) assuming:				Eruption age (ka) assuming:	
				Tg 800	RSL	Tg 700	RSL	Tg 800	Tg 700
Summit knoll #1970-R01	No uplift (0 mm/yr)	0.32	94	77	-17	80	-14	8.4	8.2
	Faster uplift (1 mm/yr)							9.0	8.9
	Faster uplift (2 mm/yr)							9.8	9.5
Crater lava #719-R14	No uplift (0 mm/yr)	0.31	106	71	-35	75	-31	9.7	9.3
	Faster uplift (1 mm/yr)							10.5	10.2
	Faster uplift (2 mm/yr)							11.1	10.9

youngest combination	oldest combination
----------------------	--------------------

*Local deformation after emplacement and quench*

In the time following lava emplacement and quench, it is possible that local deformation of the volcanic edifice could cause uplift or subsidence of the lavas (e.g. by growth of a cryptodome, or caldera subsidence). The flat summit of Oomurodashi on which these lavas occur coupled with ROV observations make us confident that this type of local uplift or subsidence has not affected these lavas since their eruption and quench. If applying this method to lavas for which post-emplacement deformation cannot be ruled out, post-emplacement uplift would lead to increased apparent ages whereas post-emplacement subsidence would lead to younger apparent ages. For reference, Table S7 compares the apparent ages for the Oomurodashi lavas assuming hypothetical uplift and subsidence of 2 and 20 m. Assuming post-emplacement deformation of  $\pm 2$  m gives a range in lava ages of  $\leq 0.6$  ka; deformation of  $\pm 20$  m gives a range of 0 – 10.5 ka for the summit knoll and 8.6 – 12.5 ka for the crater lava.

*Table S7.*

		Mean OH (wt%)	Adjusted sampling depth (mbsl)	Eruption depth (mbsl) & Relative Sea Level (m) assuming:				Eruption age (ka) assuming:	
				Tg 800	RSL	Tg 700	RSL	Tg 800	Tg 700
Summit knoll #1970-R01	20 m subsidence	0.32	74		3		6	4.7	*
	2 m subsidence		92	77	-15	80	-12	8.9	8.6
	2 m uplift		96		-19		-16	9.1	8.9
	20 m uplift		114		-37		-34	10.5	10.3
Crater lava #719-R14	20 m subsidence	0.31	86		-15		-11	8.9	8.6
	2 m subsidence		104	71	-33	75	-29	10.2	9.9
	2 m uplift		108		-37		-33	10.5	10.2
	20 m uplift		126		-55		-51	12.5	11.4

<i>youngest combination</i>	<i>oldest combination</i>	<i>* regional RSL never exceeds +3m</i>
-----------------------------	---------------------------	---

## References

- Anderson, S.W., and Fink, J.H., 1989, Hydrogen-isotope evidence for extrusion mechanisms of the Mount St Helens lava dome: *Nature*, v. 341, p. 521–523, doi:10.1038/341521a0.
- Anderson, S.W., Fink, J.H., and Rose, W.I., 1995, Mount St. Helens and Santiaguito lava domes: The effect of short-term eruption rate on surface texture and degassing processes: *Journal of Volcanology and Geothermal Research*, v. 69, p. 105–116, doi:10.1016/0377-0273(95)00022-4.
- Behrens, H., Tamic, N., and Holtz, F., 2004, Determination of the molar absorption coefficient for the infrared absorption band of CO<sub>2</sub> in rhyolitic glasses: *American Mineralogist*, v. 89, p. 301–306, doi:10.2138/am-2004-2-307.
- Chang, Q., Shibata, T., Shinotsuka, K., Yoshikawa, M., and Tatsumi, Y., 2003, Precise determination of trace elements in geological standard rocks using inductively coupled plasma mass spectrometry (ICP-MS): *Front Res Earth Evol*, v. 1, p. 357–362.
- Dingwell, D.B., and Webb, S.L., 1990, Relaxation in silicate melts: *European Journal of Mineralogy*, v. 2, p. 427–451, doi:10.1127/ejm/2/4/0427.
- Fujii, S., and Fuji, N., 1967, Postglacial Sea Level in the Japanese Islands: *Journal of Geoscience, Osaka City University*, v. 10, p. 43–51.
- Isshiki, N., 1982, Geology of the Kozushima district: Quadrangle Series, Geological Survey of Japan, p. 75.
- Isshiki, N., 1987, Geology of the Nijjima district: Quadrangle Series, Geological Survey of Japan, p. 85.
- Isshiki, N., 1978, Geology of the Toshima District: Quadrangle Series, Geological Survey of Japan, v. 110, p. 34.
- Kimura, J.-I., and Chang, Q., 2012, Origin of the suppressed matrix effect for improved analytical performance in determination of major and trace elements in anhydrous silicate samples using 200 nm femtosecond laser ablation sector-field inductively coupled plasma mass spectrometry: *Journal of Analytical Atomic Spectrometry*, v. 27, p. 1549–1559, doi:10.1039/c2ja10344c.
- Lambeck, K., Rouby, H., Purcell, A., Sun, Y., and Sambridge, M., 2014, Sea level and global ice volumes from the Last Glacial Maximum to the Holocene: *Proceedings of the National Academy of Sciences*, v. 111, p. 15296–15303, doi:10.1073/pnas.1411762111.
- Long, W., and Friedman, I., 1968, The refractive index of experimentally hydrated rhyolite glass: *American Journal of Science*, v. 53, p. 1754–1756.
- McIntosh, I.M., Nichols, A.R.L., Tani, K., and Llewellyn, E.W., 2017, Accounting for the species-dependence of the 3500 cm<sup>-1</sup> H<sub>2</sub>O infrared molar absorptivity coefficient: Implications for hydrated volcanic glasses: *American Mineralogist*, v. 102, p. 1677–1689, doi:10.2138/am-2017-5952CCBY.
- Mitchell, S.J., McIntosh, I.M., Houghton, B.F., Carey, R.J., and Shea, T., 2018, Dynamics of a powerful deep submarine eruption recorded in H<sub>2</sub>O contents and speciation in rhyolitic glass: The 2012 Havre eruption: *Earth and Planetary Science Letters*, v. 494, p. 135–147, doi:10.1016/j.epsl.2018.04.053.
- Newman, S., and Lowenstern, J.B., 2002, VOLATILECALC: A silicate melt-H<sub>2</sub>O-CO<sub>2</sub> solution model written in Visual Basic for excel: *Computers and Geosciences*, v. 28, p. 597–604,

doi:10.1016/S0098-3004(01)00081-4.

- Newman, S., Stolper, E.M., and Epstein, S., 1986, Measurement of water in rhyolitic glasses: Calibration of an infrared spectroscopic technique: *American Mineralogist*, v. 71, p. 1527–1541.
- Nichols, A.R.L., and Wysoczanski, R.J., 2007, Using micro-FTIR spectroscopy to measure volatile contents in small and unexposed inclusions hosted in olivine crystals: *Chemical Geology*, v. 242, p. 371–384, doi:10.1016/j.chemgeo.2007.04.007.
- Nowak, M., and Behrens, H., 2001, Water in rhyolitic magmas: Getting a grip on a slippery problem: *Earth and Planetary Science Letters*, v. 184, p. 515–522, doi:10.1016/S0012-821X(00)00343-5.
- Oikawa, T., and Tani, K., 2020, Eruption Ages of the Younger Stage of Toshima Volcano, Izu Islands, Japan, Based on <sup>14</sup>C Dating and Topographical Analysis: *Kazan*, v. 65, p. 1–5.
- Okuno, J., Nakada, M., Ishii, M., and Miura, H., 2014, Vertical tectonic crustal movements along the Japanese coastlines inferred from late Quaternary and recent relative sea-level changes: *Quaternary Science Reviews*, v. 91, p. 42–61, doi:10.1016/j.quascirev.2014.03.010.
- Stolper, E., 1982a, The speciation of water in silicate melts: *Geochimica et Cosmochimica Acta*, v. 46, p. 2609–2620, doi:10.1016/0016-7037(82)90381-7.
- Stolper, E.M., 1982b, Water in Silicate Glasses: An Infrared Spectroscopic Study: *Contributions to Mineralogy and Petrology*, v. 81, p. 1–17.
- Sun, W., and McDonough, W.F., 1989, Chemical and isotopic systematics of oceanic basalts: implications for mantle composition and processes, *in* Saunders, A.D. and Norry, M.J. eds., *Magmatism in the Ocean Basins*, Geological Society Special Publication, v. 42, p. 313–345, doi:10.1144/GSL.SP.1989.042.01.19.
- Takei, H., Yokoyama, T., Makishima, A., and Nakamura, E., 2001, Formation and suppression of AlF<sub>3</sub> during HF digestion of rock samples in Teflon bomb for precise trace element analyses by ICP-MS and ID-TIMS: *Proceedings of the Japan Academy, Ser. B*, v. 77, p. 13–17, doi:10.2183/pjab.77.13.
- Tanaka, R., Makishima, A., Kitagawa, H., and Nakamura, E., 2003, Suppression of Zr, Nb, Hf and Ta coprecipitation in fluoride compounds for determination in Ca-rich materials: *Journal of Analytical Atomic Spectrometry*, v. 18, p. 1458–1463, doi:10.1039/b309948b.
- Tani, K., Kawabata, H., Chang, Q., Sato, K., and Tatsumi, Y., 2005, Quantitative analyses of silicate rock major and trace elements by X-ray fluorescence spectrometer: evaluation of analytical precision and sample preparation: *Frontier Research on Earth Evolution*, v. 2, p. 1–8.
- Taylor, R.N., and Nesbitt, R.W., 1998, Isotopic characteristics of subduction fluids in an intra-oceanic setting, Izu-Bonin Arc, Japan: *Earth and Planetary Science Letters*, v. 164, p. 79–98, doi:10.1016/S0012-821X(98)00182-4.
- Uesugi, Y., Shinkawa, K., and Kigoshi, K., 1994, Tephra Outcropping along the So-called “Chisohsetudanmen” Roadcuts, Sembazaki, Izu-Oshima Volcano, Central Japan: *Standard Tephra Columns: The Quaternary Research*, v. 33, p. 165–187.
- Umitsu, M., 1991, Holocene Changes and Coastal Evolution in Japan: *The Quaternary Research*, v. 30, p. 187–196.
- Zhang, Y., Jenkins, J., and Xu, Z., 1997, Kinetics of the reaction H<sub>2</sub>O + O ⇌ 2OH in rhyolitic glasses upon cooling: Geospeedometry and comparison with glass transition: *Geochimica et*

*Cosmochimica Acta*, v. 61, p. 2167–2173, doi:10.1016/s0016-7037(97)00054-9.

Zhang, Y., Stolper, E.M., and Ihinger, P.D., 1995, Kinetics of the reaction  $\text{H}_2\text{O} + \text{O} = 2\text{OH}$  in rhyolitic and albitic glasses: Preliminary results: *American Mineralogist*, v. 80, p. 593–612.

Zhang, Y., Stolper, E.M., and Wasserburg, G.J., 1991, Diffusion of water in rhyolitic glasses: *Geochimica et Cosmochimica Acta*, v. 55, p. 441–456, doi:10.1016/0016-7037(91)90003-N.